**Nano-Micro Letters**

ISSN 2311-6706
e-ISSN 2150-5551
CN 31-2103/TB

**ARTICLE**

https://doi.org/10.1007/s40820-019-0258-0

**Cite as**
Nano-Micro Lett.
(2019) 11:28

Received: 18 January 2019
Accepted: 6 March 2019

# Hollow Nanocages of $Ni_xCo_{1-x}Se$ for Efficient Zinc–Air Batteries and Overall Water Splitting

Zhengxin Qian[1], Yinghuan Chen[2], Zhenghua Tang[2,3] ✉, Zhen Liu[4], Xiufang Wang[1], Yong Tian[1] ✉, Wei Gao[1] ✉

✉ Zhenghua Tang, zhht@scut.edu.cn; Yong Tian, tian_yong_tian@163.com; Wei Gao, gygaowei@126.com

[1] School of Pharmacy, Guangdong Pharmaceutical University, Guangzhou 510006, Guangdong, People's Republic of China

[2] Guangzhou Key Laboratory for Surface Chemistry of Energy Materials, New Energy Research Institute, School of Environment and Energy, South China University of Technology, Guangzhou Higher Education Mega Center, Guangzhou 510006, Guangdong, People's Republic of China

[3] Guangdong Engineering and Technology Research Center for Surface Chemistry of Energy Materials, School of Environment and Energy, South China University of Technology, Guangzhou Higher Education Mega Centre, Guangzhou 510006, Guangdong, People's Republic of China

[4] Department of Physics and Engineering, Frostburg State University, Frostburg, MD 21532-2303, USA

## HIGHLIGHTS

- A facile strategy for fabricating $Ni_xCo_{1-x}Se$ hollow nanocages was developed, and the formation mechanism was well explained.
- $Ni_{0.2}Co_{0.8}Se$ outperformed a Pt/C + $RuO_2$ catalyst in rechargeable and all-solid-state Zn–air battery tests, as well as in overall water splitting.
- The hydrogen adsorption onto $Ni_xCo_{1-x}Se$ was simulated, and Gibbs free energies were calculated.

**ABSTRACT** Developing Earth-abundant, highly efficient, and anti-corrosion electrocatalysts to boost the oxygen evolution reaction (OER), oxygen reduction reaction (ORR), and hydrogen evolution reaction (HER) for the Zn–air battery (ZAB) and for overall water splitting is imperative. In this study, a novel process starting with $Cu_2O$ cubes was developed to fabricate hollow $Ni_xCo_{1-x}Se$ nanocages as trifunctional electrocatalysts for the OER, ORR, and HER and a reasonable formation mechanism was proposed. The $Ni_{0.2}Co_{0.8}Se$ nanocages exhibited higher OER activity than its counterparts with the low overpotential of 280 mV at 10 mA cm$^{-2}$. It also outperformed the other samples in the HER test with a low overpotential of 73 mV at 10 mA cm$^{-2}$. As an air–cathode of a self-assembled rechargeable ZAB, it exhibited good performance, such as an ultralong cycling lifetime of > 50 h, a high round-trip efficiency of 60.86%, and a high power density of 223.5 mW cm$^{-2}$. For the application in self-made all-solid-state ZAB, it also demonstrated excellent performance with a power density of 41.03 mW cm$^{-2}$ and an open-circuit voltage of 1.428 V. In addition, $Ni_{0.2}Co_{0.8}Se$ nanocages had superior performance in a practical overall water splitting, in which only 1.592 V was needed to achieve a current density of 10 mA cm$^{-2}$. These results show that hollow $Ni_xCo_{1-x}Se$ nanocages with an optimized Ni-to-Co ratio are a promising cost-effective and high-efficiency electrocatalyst for ZABs and overall water splitting in alkaline solutions.

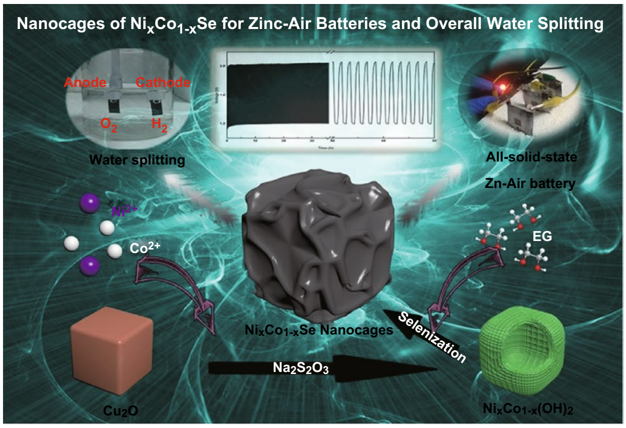

**KEYWORDS** $Ni_xCo_{1-x}Se$ hollow nanocages; Oxygen evolution reaction; Hydrogen evolution reaction; Rechargeable/all-solid-state zinc–air battery; Overall water splitting

## 1 Introduction

The rapid depletion and heavy reliance on fuel cells and associated global environmental concerns have motivated extensive research on the development of eco-friendly and sustainable energy technologies in the past decade. Among these technologies, Zn–air batteries (ZABs) and water-splitting devices have become viable eco-friendly energy technologies owing to recent advances in the preparation of highly active electrocatalysts [1–3]. The oxygen evolution reaction (OER) and oxygen reduction reaction (ORR) are the key reversible reactions occurring at the cathode of ZABs and largely determine the energy-conversion efficiency of ZABs [4]. The OER and the hydrogen evolution reaction (HER) are the two electrochemical reactions for catalyzing overall water splitting [5–7]. Pt-based materials have been widely considered as state-of-the-art electrocatalysts for the ORR and HER [8–12], while $RuO_2$ and $IrO_2$ are the standard high-efficiency OER catalysts [13, 14]. However, the large-scale commercial implementation of both Pt-based and Ru-/Ir-based materials has been significantly hampered by their scarcity, high cost, and poor long-term durability. Therefore, it is imperative to develop Earth-abundant, cost-effective, high-efficiency, and robust electrocatalysts [12, 15–24].

Among the various alternative materials, transition metal chalcogenides have been attracting increasing research attention, mainly owing to their high availability, low cost, and eco-friendliness [25–32]. In particular, because of the high conductivity of metallic Se compared with O and S, transition metal selenides (MSe, M = transition metal) have superior electrocatalytic performance to transition metal oxides and sulfides [30, 31]. Therefore, transition metal selenides have received tremendous research attentions from the electrocatalytic community. For instance, Zheng et al. developed a novel hot-injection process to precisely control the phase and composition of a series of $Ni_xSe$ nanocrystals and discovered that $Ni_{0.5}Se$ nanoparticles exhibited superior OER activity comparable to that of $RuO_2$, that $Ni_{0.75}Se$ nanoparticles exhibited the best performance for the HER and ORR, and that both could be engineered for efficient rechargeable ZABs and water splitting [33]. Cao et al. demonstrated a facile strategy for in situ coupling of ultrafine $Co_{0.85}Se$ nanocrystals with N-doped C, and the as-prepared $Co_{0.85}Se$@NC was employed as a trifunctional catalyst for the HER, ORR, and OER, exhibiting great potential for ZABs and water splitting [34]. Rather than using only one transition metal, recent studies showed that superior electrocatalytic performance for ZABs and water splitting could be achieved by employing mixed transition metal selenides. For example, Xu et al. [35] prepared a Ni–Fe diselenide ($Ni_xFe_{1-x}Se_2$) and used it as a templating precursor to form ultrathin nanosheets of the corresponding oxide, which exhibited a very low overpotential of only 195 mV in an alkaline solution at 10 mA $cm^{-2}$ for the OER. Recently, Lv et al. [36] have designed Ni–Fe selenide ($NiFeSe_2$) hollow nanoparticles, hollow nanochains [37], and Co–Fe selenide ($CoFeSe_2$) nanosheets [38] for the OER, and the $Co_{0.4}Fe_{0.6}Se$ nanosheets not only exhibited superior OER performance with a low overpotential of 217 mV at 10 mA $cm^{-2}$ and a small Tafel slope of 41 mV $dec^{-1}$ but also had a ultrahigh durability. There have been several reports of $NiCoSe_2$-based materials for electrochemical energy storage and conversion. Yuan et al. reported monodisperse metallic $NiCoSe_2$ hollow sub-microspheres for electrochemical supercapacitors [39]. $NiCoSe_{2-x}$/N-doped C mushroom-like core/shell nanorods on N-doped C fiber were prepared by Li et al. [40] for overall water splitting, and a low cell voltage of 1.53 V to obtain a current density of 10 mA $cm^{-2}$ was observed. Recently, Chen and Tan have directly grew ultrathin ternary selenide ($CoNiSe_2$) nanorods on Ni foam, which delivered a current density of 100 mA $cm^{-2}$ with an overpotential as low as 307 and 170 mV for the OER and HER, respectively, and eventually reduced the cell voltage in the full water-splitting reaction to 1.591 V to obtain a current density of 10 mA $cm^{-2}$ [41]. Chen and Wang groups prepared a three-dimensional Ni–Co selenide ($NiCoSe_2$) nanonetwork for the OER, and the overpotential at 10 mA $cm^{-2}$ was 274 mV, exhibiting room for improvement [42].

Despite the progress regarding $NiCoSe_2$, direct preparation of $NiCoSe_2$ with precise manipulation of the morphology for ZABs and overall water splitting remains largely unexplored. Moreover, the stoichiometric ratio of Ni to Co has not been optimized for enhancing the synergistic catalytic effects. In light of the significant effects of the morphology, crystal structure, and stoichiometry on the electrocatalytic performance, a systematic investigation of $NiCoSe_2$ with a well-defined surface structure and an optimized Ni/Co stoichiometry for establishing the structure–function relationship of $NiCoSe_2$ materials is of great importance. This was the primary goal of the present study.

https://doi.org/10.1007/s40820-019-0258-0

In this study, we employed a facile strategy to prepare a series of $Ni_xCo_{1-x}Se$ samples with hollow cages and investigated them as trifunctional electrocatalysts for the OER, ORR, and HER. A novel process with $Cu_2O$ cubes as the starting material was developed to fabricate the $Ni_xCo_{1-x}Se$ nanocages, and a reasonable formation mechanism was proposed. In electrochemical tests, $Ni_{0.2}Co_{0.8}Se$ exhibited higher OER and HER activity than the other samples in the $Ni_xCo_{1-x}Se$ series. To investigate the applications of the $Ni_{0.2}Co_{0.8}Se$ sample, it was used as an air–cathode of a self-assembled rechargeable ZAB and an all-solid-state ZAB and employed as a catalyst for overall water splitting in an alkaline solution.

## 2 Experimental Section

### 2.1 Materials

Copper (II) chloride dihydrate ($CuCl_2·2H_2O$, 99%), sodium hydroxide (NaOH, ≥ 96.0%), *L*-ascorbic acid (AA, ≥ 99.7%), nickel (II) chloride hexahydrate ($NiCl_2·6H_2O$, ≥ 98.0%), cobalt (II) chloride hexahydrate ($CoCl_2·6H_2O$, ≥ 99.0%), polyvinylpyrrolidone (PVP, K30, 99%), anhydrous sodium thiosulfate ($Na_2S_2O_3$, 99%), sodium selenite ($Na_2SeO_3$, ≥ 99.7%), absolute ethanol (≥ 99.7%), and ethylene glycol (EG, 99.0%) were used. Water was obtained from a Barnstead Nanopure water system (resistivity: 18.3 MΩ cm). All the chemicals were used as received, without further purification.

### 2.2 Synthesis of $Cu_2O$ Cubes

$Cu_2O$ cubes were synthesized by following a previously reported procedure [43]. Typically, 341 mg of $CuCl_2·2H_2O$ was first dissolved in 200 mL of Nanopure water. Then, the solution was heated to 55 °C and stirred for 30 min. Subsequently, 20 mL of a 2 M NaOH solution was slowly added to the aforementioned solution, forming a brown suspension. After 10 min of stirring, 20 mL of 0.6 M AA was added dropwise to the solution. The solution gradually changed from dark red to brick red, and the mixture was aged for 3 h. The formed precipitates were collected via suction filtration, washed with copious distilled water and ethanol 3–5 times, and eventually dried in vacuum at 35 °C overnight.

### 2.3 Synthesis of $Ni_{0.2}Co_{0.8}(OH)_2$ Nanocages

In a typical procedure, 100 mg of cuprous oxide was dissolved into a mixed solvent of absolute ethanol and Nanopure water (100 mL, volume ratio = 1:1) with 30 min of ultrasonic treatment. Then, 34 mg of $NiCl_2·6H_2O$ and $CoCl_2·6H_2O$ (molar ratio of 2:8) was added to the solution, with stirring. Subsequently, 3.33 g of PVP was dispersed in the resulting suspension under another 30 min of ultrasonic treatment. Then, 40 mL of 1 M $Na_2S_2O_3$ was slowly added to the mixture. Upon the addition of an excessive amount of sodium thiosulfate solution, the mixture changed from orange–red to transparent green, indicating that cuprous oxide was converted into $Ni_{0.2}Co_{0.8}(OH)_2$. The reaction was conducted for 10 min to ensure that it was complete. The product was then collected via centrifugation, washed with copious Nanopure water and ethanol 3–5 times, and eventually dried in a vacuum at 35 °C overnight. For the synthesis of $Ni_{0.5}Co_{0.5}(OH)_2$, $Ni_{0.8}Co_{0.2}(OH)_2$, $Ni(OH)_2$, and $Co(OH)_2$, the same procedure was adopted, but the molar ratio of Ni to Co was changed to 5:5, 8:2, 1:0, and 0:1, respectively.

### 2.4 Synthesis of $Ni_{0.2}Co_{0.8}Se$ Nanocages

In a typical procedure, 37 mg of $Na_2SeO_3$ was dissolved in a mixed solvent of Nanopure water and EG (10.0 mL, volume ratio = 1:1). Then, 10 mg of $Ni_{0.2}Co_{0.8}(OH)_2$ was added to the solution, with 30 min of ultrasonication to ensure uniform dispersion. Subsequently, the mixture was transferred into an autoclave and kept at 200 °C for 6 h. Finally, after cooling to room temperature, the product was collected via centrifugation.

### 2.5 Characterization

The morphologies and surface structures of the samples were observed via field emission scanning electron microscopy (SEM, Hitachi S-4800) and high-resolution transmission electron microscopy (HRTEM, Tecnai G2 F30). X-ray diffraction (XRD) patterns in the Bragg's angle ($2\theta$) range of 10°–90° were recorded using a Bruker D8 diffractometer with Cu $K_\alpha$ radiation ($\lambda = 0.1541$ nm). X-ray photoelectron spectroscopy (XPS) was conducted using an ESCALAB 250 photoelectron spectrometer (Thermo Fisher Scientific, USA).

### 2.6 Electrochemistry

Electrochemical measurements were taken using a CHI 750E electrochemical workstation (CHI Instruments Inc.) in a 1 M KOH aqueous solution at ambient temperature. A three-electrode system was utilized in both HER and OER tests. Here, Ag/AgCl was used as the reference electrode [44–46], and C rod and C cloth electrodes were employed as the counter electrode and the working electrode, respectively. The catalyst ink was prepared as follows. Firstly, 10 mg of the catalyst was ultrasonically dispersed in 1000 µL of absolute ethanol, followed by the sequential addition of 900 µL of Nanopure water and 100 µL of Nafion (5%, Sigma-Aldrich), yielding a uniform suspension. Then, 20 µL of the suspension was cast dropwise onto a single-sided C cloth ($1.5\times0.5$ cm$^2$, load area of 0.5 cm$^2$), followed by drying at room temperature. The catalyst loading was calculated as ~ 200 µg cm$^{-2}$. The solution was saturated with $N_2$ or $O_2$ at least 30 min before each measurement. For the HER, the cyclic voltammetry (CV) test potential range was − 0.077 to 0.623 V (vs. reversible hydrogen electrode (RHE)), and the scan rate was 100 mV s$^{-1}$. In addition, linear sweep voltammetry (LSV) was conducted in a potential range of − 0.477 to 0.323 V (vs. RHE), at a scan rate of 10 mV s$^{-1}$. OER measurements were taken in the same manner as the HER measurements. LSV was performed in a $N_2$-saturated 1 M KOH solution within the potential range of + 1.023 to + 2.023 V (vs. RHE), at a scan rate of 10 mV s$^{-1}$. A relatively simple two-electrode system was used in the water-splitting test, where the same catalyst was loaded on two clip electrodes: an anode and a cathode. The operation method was similar to that for the OER test, but the LSV test voltage was 1.0–2.0 V. We recorded the chronoamperometric responses in a 1 M KOH solution for 40,000 s and performed an accelerated durability test (ADT), where the catalyst was cycled 1000 times in the potential range of + 1.023 to + 1.423 V (vs. RHE) for the OER and from − 0.077 to 0.623 V for the HER. The scan rates for the HER and OER were 100 and 50 mV s$^{-1}$, respectively. Details regarding the calculation of the electrochemically active surface area (EASA) are presented in Supplementary Material.

### 2.7 Measurements of Liquid ZAB and All-Solid-State ZAB

In the rechargeable ZAB test, a Zn sheet (thickness of 0.5 mm) was used as the anode, the C cloth loaded with the catalyst was employed as the air–cathode, and 6 M KOH + 0.2 M ZnAc was used as the electrolyte. The procedure for preparing the catalyst ink was as follows. First, 3 mg of the sample was dispersed in 700 µL of a Nafion solution (70 µL of Nafion in 630 µL of absolute ethanol), followed by ultrasonication for 15 min. Subsequently, 600 µL of the catalyst was loaded on a C cloth, and the loading area was approximately 1 cm$^2$. For the preparation of Pt/C + $RuO_2$ as the control, 1.5 mg of commercial Pt/C and 1.5 mg of $RuO_2$ were mixed in 630 µL of absolute ethanol, and then, 70 µL of Nafion was added. After 30 min of ultrasonication, 600 µL of the dispersion was employed for a control test. A ZAB test was performed at room temperature using a CHI-440 electrochemical workstation (CHI Instruments Inc.). LSV was conducted in the voltage range of 0.3–2.7 V at a scan rate of 10 mV s$^{-1}$. The galvanostatic charge–discharge cycling curves were recorded at 10 mA cm$^{-2}$ via chronopotentiometry, with 5 min of discharging and 5 min of charging. The electrochemical test method for the all-solid-state ZAB was similar to that for the liquid ZAB, with the differences being the electrolyte and the thickness of the Zn sheet (0.3 mm). The preparation method for the polyvinyl alcohol (PVA) electrolyte gel was as follows. Firstly, 666 mg of PVA-1788 and 333 mg of PVA-1799 were placed in a flask, and then, 10 mL of 6 M KOH + 0.2 M ZnAc was added. The mixture was kept under magnetic stirring at room temperature for 1 h and then transferred into an oil bath at 95 °C for 30 min. Subsequently, it was poured into a mold while being hot, frozen in a -70 °C refrigerator for 1 h, and finally removed and defrosted at 2 °C for 4 h to obtain the electrolyte gel. The catalyst loading was approximately 2 mg cm$^{-2}$ for the all-solid-state ZAB test. The discharge power density was determined via LSV and calculated as Eq. 1 [47].

$$\text{Power density}\left(\text{mW cm}^{-2}\right) = \text{Voltage} \times \text{Current density} \tag{1}$$

The specific capacity was determined using the galvanostatic discharge plot and calculated as Eq. 2.

$$\text{Specific capacity}\left(\text{mAh g}^{-1}\right) = \frac{\text{Current} \times \text{Service hours}}{\text{Weight of consumed Zn}}. \tag{2}$$

## 3 Results and Discussion

### 3.1 Preparation of $Ni_xCo_{1-x}Se$ Nanocages, Formation Mechanism, and Electron Microscopy

Figure 1a shows schematics of the fabrication process for the $Ni_xCo_{1-x}Se$ nanocages. Firstly, $Cu_2O$ nanocubes were synthesized by following a previously reported procedure [43]. Subsequently, in the presence of $NaS_2O_3$, the $Cu_2O$ reacted with $Co^{2+}$ and $Ni^{2+}$ ions to form NiCo hydroxide. After the selenization of the NiCo hydroxide, $Ni_xCo_{1-x}Se$ nanocages were formed. SEM and TEM images of the $Cu_2O$, $Ni_{0.2}Co_{0.8}(OH)_2$, and $Ni_{0.2}Co_{0.8}Se$ are shown in Fig. 1b–d. The $Cu_2O$ exhibited a well-defined cube shape, with some cubes clustered together. These well-defined cube morphologies are clearly recognized in $Ni_{0.2}Co_{0.8}(OH)_2$, despite the numerous fine flocci appearing on the surface. To examine the structure of $Ni_{0.2}Co_{0.8}(OH)_2$, we conducted XRD, energy-dispersive X-ray spectroscopy (EDX), and Fourier transform infrared (FT-IR) spectroscopic measurements (Fig. S1). The XRD results indicate that the $Ni_{0.2}Co_{0.8}(OH)_2$ had an amorphous structure. Similar preparations and structures of $Ni_xCo_{1-x}(OH)_2$ have been well documented [43, 48]. According to the EDX results, the atomic ratio of Ni to Co was 18.26:81.74, which is approximately 2:8. In the FT-IR spectrum, the broadband at 3447 $cm^{-1}$ can be assigned to the stretching vibration of O–H groups, which were hydrogen-bonded to $H_2O$ molecules in the interlayer space. The band centered at 662 $cm^{-1}$ is ascribed to $\delta$(Ni–O–H), and the absorption band at 459 $cm^{-1}$ is attributed to $\upsilon$(Co/Ni–O) stretching vibrations [39]. Together, the results of XRD, EDX, and FT-IR confirm that $Ni_{0.2}Co_{0.8}(OH)_2$ with an amorphous structure was successfully prepared. For $Ni_{0.2}Co_{0.8}Se$, hollow nanocages were observed, and their detailed surface structure was examined via HRTEM, as discussed later. The size evolution was monitored throughout the fabrication process, and the size distribution histograms are presented in Fig. S2. The average length of the $Cu_2O$ cubes, $Ni_{0.2}Co_{0.8}(OH)_2$ nanocages, and $Ni_{0.2}Co_{0.8}Se$ nanocages was approximately 509.2 ± 140.6, 573.8 ± 157.7, and 429.6 ± 85.1 nm, respectively, indicating that the size was not significantly changed by the chemical treatments as shown in Eqs. 3–7.

$$Cu_2O + xS_2O_3^{2-} + H_2O \rightarrow \left[Cu_2(S_2O_3)_x\right]^{2-2x} + 2OH^- \quad (3)$$

$$xNi^{2+} + (1-x)Co^{2+} + 2OH^- \rightarrow Ni_xCo_{1-x}(OH)_2 \quad (4)$$

$$2SeO_3^{2-} + CH_2OHCH_2OH \rightarrow 2Se + H_2C_2O_4 + 4OH^- \quad (5)$$

$$3Se + 6OH^- \rightarrow 2Se^{2-} + SeO_3^{2-} + 3H_2O \quad (6)$$

$$Se^{2-} + Ni_xCo_{1-x}(OH)_2 \rightarrow Ni_xCo_{1-x}Se + 2OH^- \quad (7)$$

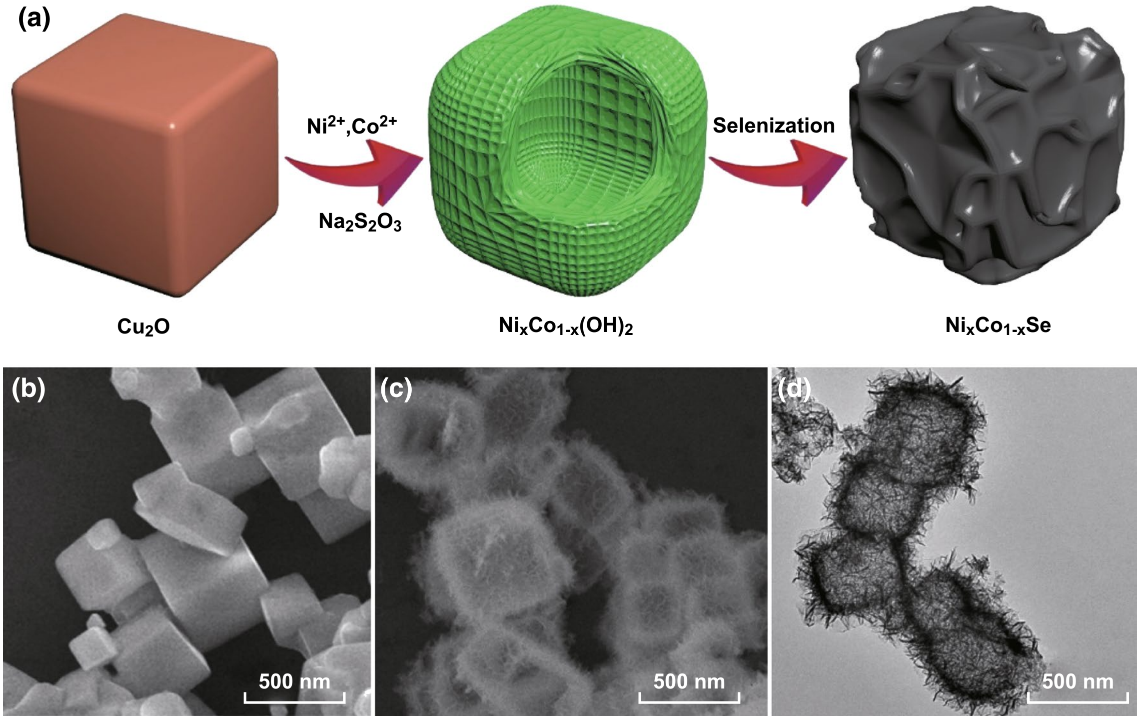

**Fig. 1** **a** Schematics of the fabrication process for the $Ni_xCo_{1-x}Se$ nanocages. Representative SEM images of **b** the $Cu_2O$ cubes and **c** the $Ni_{0.2}Co_{0.8}(OH)_2$ nanocages. **d** Representative TEM image of the $Ni_{0.2}Co_{0.8}Se$ nanocages

A possible mechanism for the formation of hollow $Ni_xCo_{1-x}Se$ nanocages is described as follows. According to the Pearson's hard and soft acid–base principle, cuprous oxide can react with sodium thiosulfate to form a soluble complex, accompanied by the release of hydroxide ions (Eq. 3). In the presence of hydroxide ions, upon the introduction of Ni and Co ions, the immediately formed NiCo hydroxide precipitates can aggregate in situ, leading to the formation of $Ni_xCo_{1-x}(OH)_2$ nanocages (Eq. 4). The selenization proceeds via an anion exchange mechanism. Under a high temperature and high pressure, EG can react with $SeO_3^{2-}$, generating elemental Se, hydroxide ions, and oxalic acid (Eq. 5). In the presence of hydroxide ions, the elemental Se can undergo the disproportionation reaction, forming $SeO_3^{2-}$ and $Se^{2-}$ (Eq. 6). Finally, the generated $Se^{2-}$ and the $OH^-$ ions complete the anion exchange reaction, forming the $Ni_xCo_{1-x}Se$ nanocages (Eq. 7).

Figure 2a, b presents typical TEM images of the $Ni_{0.2}Co_{0.8}Se$ nanocages with different magnifications. The hollow cube cage morphology is clearly observed. On the surface of the cages, there were numerous flocci, some of which were stacked or intersected together. According to the HRTEM image in Fig. 2c, the lattice spacing was 0.272 nm, which can be assigned to the crystal phase of NiCo (101). A representative high-angle annular dark-field imaging scanning TEM (HAADF-STEM) image of an $Ni_{0.2}Co_{0.8}Se$ particle is shown in Fig. 2d, where a well-defined cage shape is clearly observed. The corresponding elemental mapping images of Ni, Co, and Se in Fig. 2e–g indicate that the three elements were homogeneously distributed with excellent uniformity, and all the elements had higher densities on the edges than in the core. These results confirm that the hollow nanocages of $Ni_{0.2}Co_{0.8}Se$ were acquired via our designed strategy. Additionally, the atomic percentages were approximately determined using the EDX spectrum. As illustrated in Fig. S3, the calculated Ni–Co–Se atomic ratio was 10.03:38.90:50.07, which corresponds well to the initial loading molar ratio of 0.2:0.8:1.

## 3.2 XRD and XPS Analyses

XRD measurements were taken to further elucidate the crystal structure of the $Ni_xCo_{1-x}Se$ samples. In Fig. 3a, the series

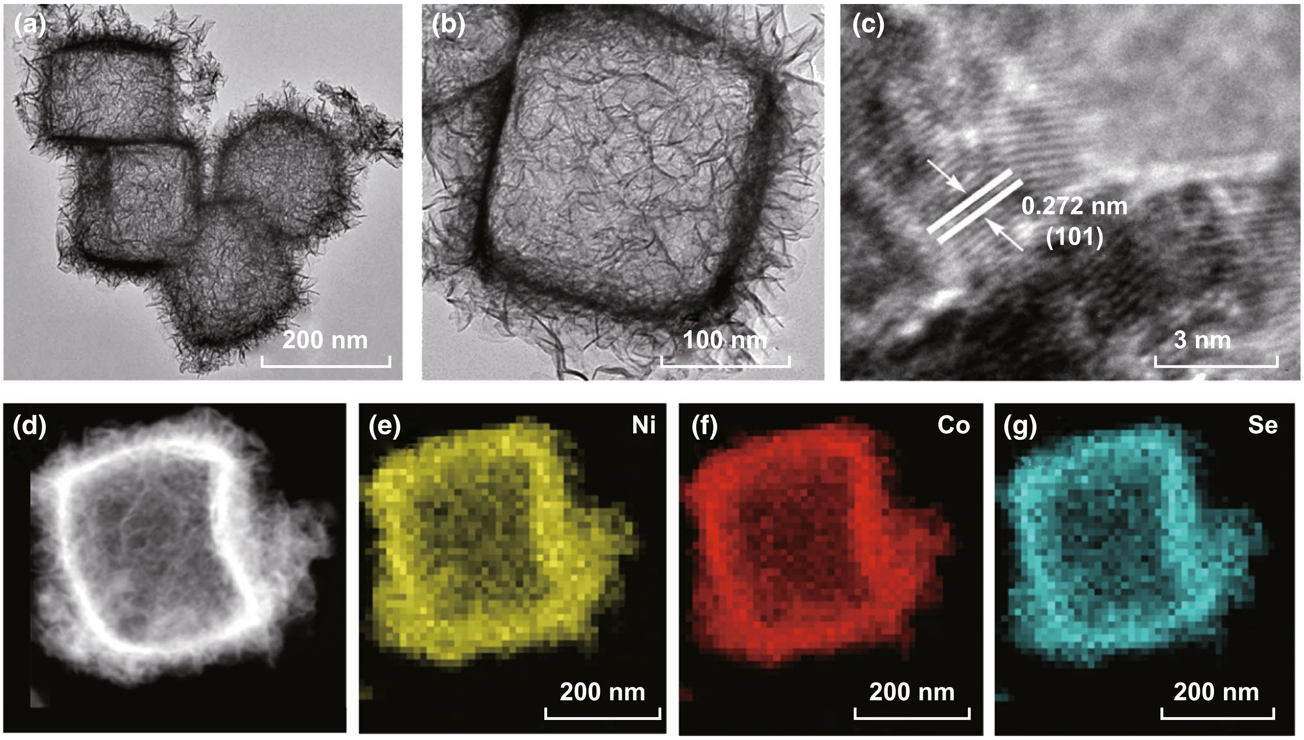

**Fig. 2** **a**–**c** Representative TEM and HRTEM images of the $Ni_{0.2}Co_{0.8}Se$ nanocages. **d** HAADF-STEM image of $Ni_{0.2}Co_{0.8}Se$ and **e**–**g** the corresponding elemental mapping images of Ni, Co, and Se

of peaks at 32.9°, 44.6°, 50.3°, 59.6°, 61.5°, and 69.1° for $Ni_{0.2}Co_{0.8}Se$ are in good accordance with the standard card of $NiCoSe_2$ (JCPDS No. 70-2851), and these Bragg reflections can be assigned to the crystal phases of (101), (102), (110), (103), (201), and (202), respectively [39, 41, 49]. The XRD patterns of the other samples in the series, along with NiSe and CoSe, are shown in Fig. S4. $Ni_{0.5}Co_{0.5}Se$ and $Ni_{0.8}Co_{0.2}Se$ exhibit patterns similar to those of $Ni_{0.2}Co_{0.8}Se$, and the patterns for NiSe and CoSe agree well with the previously recorded feature [33, 34]. The peak of $Ni_{0.2}Co_{0.8}Se$ is slightly offset from that of the standard card. As the Co ratio increases, the XRD peak position moves toward a larger diffraction angle, indicating that Co atoms were successfully doped into the $Ni_{0.5}Co_{0.5}Se$ (same as the $NiCoSe_2$ standard) lattice (Fig. S4). In contrast, the XRD peak of $Ni_{0.8}Co_{0.2}Se$ had a smaller diffraction angle than that of $Ni_{0.5}Co_{0.5}Se$ (Fig. S4). This strongly indicates the formation of $Ni_{0.2}Co_{0.8}Se$ ternary compounds rather than a mixture of two solid phases. Because $Ni_{0.2}Co_{0.8}Se$, $Ni_{0.5}Co_{0.5}Se$, and $Ni_{0.8}Co_{0.2}Se$ had the same hexagonal crystal structure and similar lattice parameters, the $Ni_{0.5}Co_{0.5}Se$ compound was intentionally prepared as a reference, and its diffraction pattern fully matched the standard card of JCPDS No. 70-2851. The results indicate that the designed method for preparing the compounds was rational and successful. Such subtle manipulation of the lattice through the optimization of the substrate elements has been previously reported [33, 43].

Subsequently, the chemical states of the composites were investigated via XPS, and the spectra are shown in Fig. 3b–d. In Fig. 3b, the two striking peaks with binding energies of 873.1 and 855.2 eV and the two satellite peaks can be assigned to the Ni $2p_{1/2}$ and Ni $2p_{3/2}$ electrons, respectively, strongly indicating that elemental Ni existed as Ni(II) [39]. In Fig. 3c, the Co $2p_{1/2}$ and Co $2p_{3/2}$ signals (797.4 and 781.3 eV) and two satellite peaks are characteristics of Co(II) [39]. The high-resolution Se 3*d* spectra can be deconvoluted

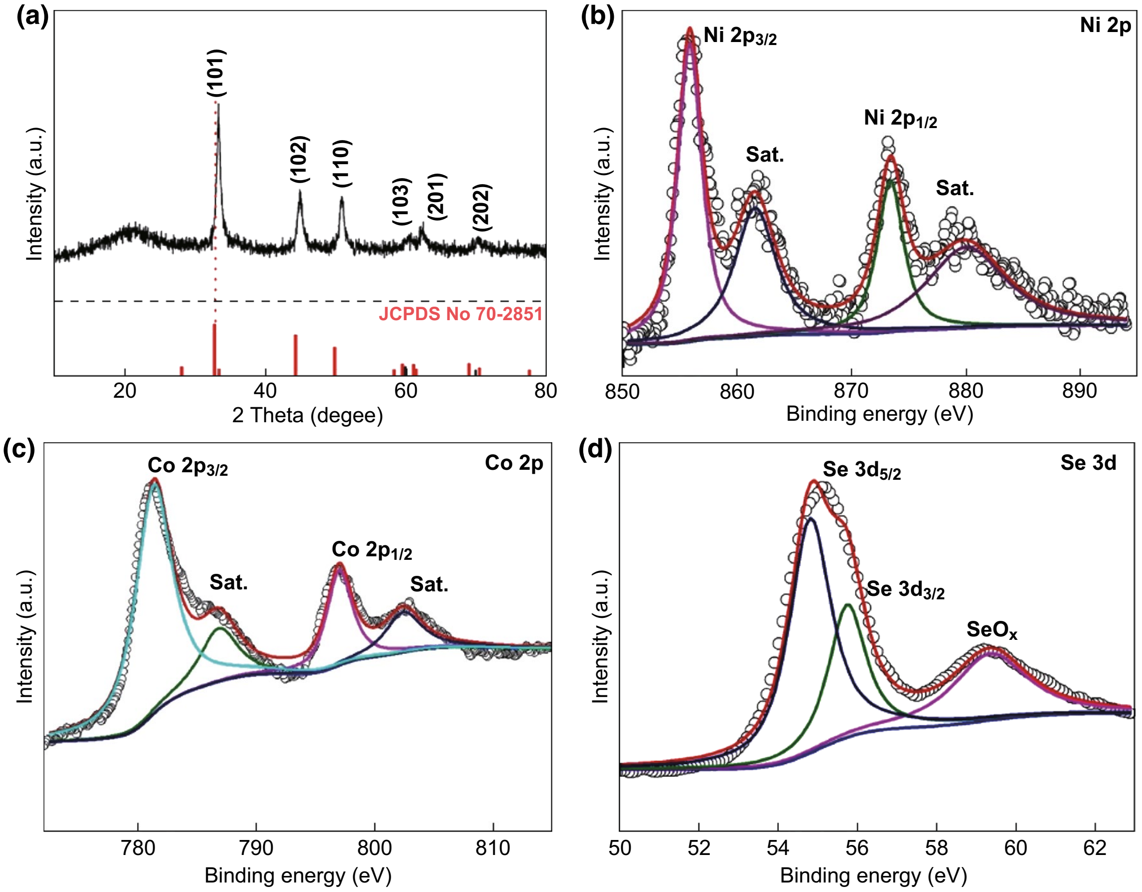

**Fig. 3** **a** XRD pattern of the $Ni_{0.2}Co_{0.8}Se$ nanocages. The core-level XPS spectra for the **b** Ni 2*p*, **c** Co 2*p*, and **d** Se 3*d* electrons of $Ni_{0.2}Co_{0.8}Se$

into two peaks at 55.6 and 54.8 eV, which correspond well to the Se $3d_{3/2}$ and Se $3d_{5/2}$ electrons, respectively. Interestingly, the peak at 59.3 eV indicates the formation of $SeO_x$, which was probably due to the surface oxidation of selenide [49].

The high-resolution XPS spectra of the Ni 2*p*, Co 2*p*, and Se 3*d* electrons of $Ni_{0.5}Co_{0.5}Se$, $Ni_{0.8}Co_{0.2}Se$, NiSe, and CoSe are shown in Fig. S5. In the Ni 2*p* spectrum (S5c1) and the NiSe and Co 2*p* (S5d1) spectrum for CoSe, the binding energies correspond to the Ni(II) and Co(II) species. For $Ni_{0.5}Co_{0.5}Se$, there are two distinctive peaks at 855.6 and 873.4 eV in the Ni 2*p* spectrum (S5a1), and both binding energy values correspond to the chemical valences exhibited by the Ni element in $Ni_{0.2}Co_{0.8}Se$, suggesting the presence of Ni(II). In the Co 2*p* spectrum (S5a2), the two sharp peaks (Co $2p_{3/2}$ and Co $2p_{1/2}$) at 781.2 and 797.9 eV are attributed to the Co(II) species. For $Ni_{0.8}Co_{0.2}Se$, the core-level Ni 2*p* spectrum (S5b1) exhibits two peaks at 855.4 and 873.3 eV, which are indexed to the Ni $2p_{3/2}$ and Ni $2p_{1/2}$ electrons, respectively, and there are two corresponding shakeup satellite peaks at 861.6 and 880.1 eV. The Co 2*p* spectrum (S5b2) exhibits a similar feature to the Co 2*p* spectrum for CoSe, implying that the Co exists as Co(II). Furthermore, the core-level Se 3*d* spectra (S5a3, b3, c2, and d2) of $Ni_{0.5}Co_{0.5}Se$, $Ni_{0.8}Co_{0.2}Se$, NiSe, and CoSe all exhibit two distinct characteristic peaks around 55.1 and 59.3 eV. The peak at 55.1 eV can be fitted into two sub-peaks representing the Se $3d_{5/2}$ and Se $3d_{3/2}$ electrons from the Se element. The other peak at 59.3 eV is probably due to the oxidation of surface Se and the formed Se–O bonds [49].

### 3.3 OER Performance

The electrochemical properties of the $Ni_xCo_{1-x}Se$ series toward the OER were examined, and the electrocatalytic performance is compiled in Table 1. Figure 4a shows the LSV curves of the $Ni_xCo_{1-x}Se$ series, NiSe, and CoSe tested in $N_2$-saturated 1 M KOH. With the decrease in the Ni percentage in the total transition metal, the OER activity gradually intensified. The $Ni_{0.2}Co_{0.8}Se$ sample exhibited the best activity. NiSe had negligible OER activity, whereas the performance of CoSe was only slightly inferior to that of $Ni_{0.2}Co_{0.8}Se$. For obtained current density of 10 mA $cm^{-2}$, the required overpotential was 280, 360, 350, and 345 mV for $Ni_{0.2}Co_{0.8}Se$, $Ni_{0.5}Co_{0.5}Se$, $Ni_{0.8}Co_{0.2}Se$, and CoSe, respectively. $Ni_{0.2}Co_{0.8}Se$ exhibited the best OER activity in the series, and its OER activity was markedly superior to that of the benchmark $IrO_2$ catalyst for the OER (Fig. S6, overpotential of 354 mV at 10 mA $cm^{-2}$). The corresponding Tafel plots are presented in Fig. 4b, where the Tafel slope can be extrapolated and calculated. As expected, NiSe exhibited the largest slope of 225.6 mA $cm^{-1}$, owing to the sluggish reaction kinetics. The Tafel slope was 86.8, 98, 95.2, and 89.3 mV $dec^{-1}$ for $Ni_{0.2}Co_{0.8}Se$, $Ni_{0.5}Co_{0.5}Se$, $Ni_{0.8}Co_{0.2}Se$, and CoSe, respectively. $Ni_{0.2}Co_{0.8}Se$ had the lowest value in the series, which was lower than that of the benchmark $IrO_2$ catalyst (117.6 mV $dec^{-1}$), indicating fast reaction kinetics. Electrochemical impedance spectroscopy (EIS) was then conducted, as shown in Fig. 4c. NiSe exhibited a near-straight line in the wide potential widow, in good accordance with its weak OER activity. Among the $Ni_xCo_{1-x}Se$ compounds, $Ni_{0.2}Co_{0.8}Se$ exhibited the smallest semicircle, indicating that it had the lowest electron-transfer resistance. Lastly, the long-term stability of $Ni_{0.2}Co_{0.8}Se$ toward the OER was examined, as shown in Fig. 4d. According to the chronoamperometric *i*–*t* curve, 82.56% of the initial current was retained after continuous testing for 10 h. Additionally, as shown in the inset of Fig. 4d, after 1000 cycles of potential scans, an extremely low additional

**Table 1** OER and HER activity for the $Ni_xCo_{1-x}Se$ series, including the results of OER and HER tests in 1 M KOH, as well as the electrochemical properties

| Sample | OER (1 M KOH) Overpotential @ 10 mA $cm^{-2}$ (mV) | HER (1 M KOH) Overpotential @10 mA $cm^{-2}$ (mV) | $C_{DL}$ (mF) | EASA ($cm^2$) |
|---|---|---|---|---|
| $Ni_{0.2}Co_{0.8}Se$ | 280 | 73 | 24.13 | 603.25 |
| $Ni_{0.5}Co_{0.5}Se$ | 360 | 112 | 1.87 | 46.75 |
| $Ni_{0.8}Co_{0.2}Se$ | 350 | 93 | 2.62 | 65.50 |
| NiSe | 390 | 150 | 0.52 | 13.00 |
| CoSe | 345 | 99 | 3.13 | 78.25 |

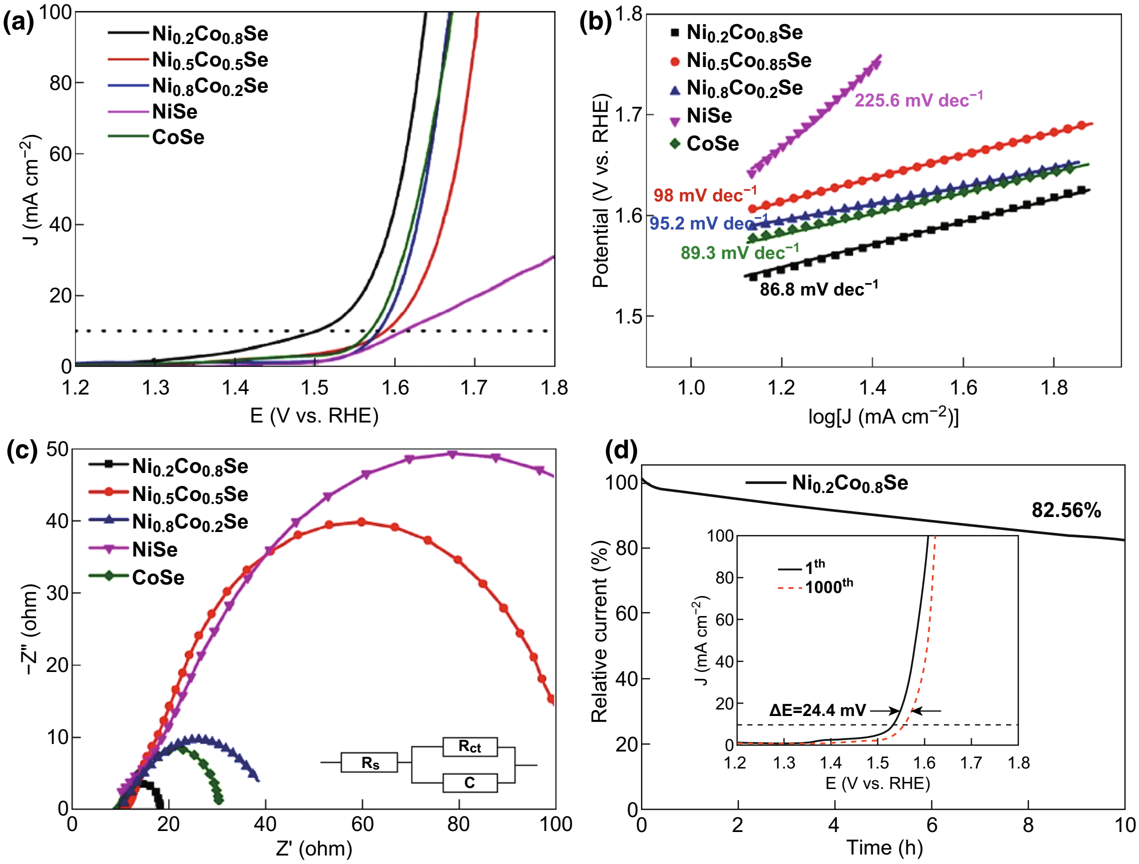

**Fig. 4** **a** IR-corrected LSV curves of $Ni_{0.2}Co_{0.8}Se$, $Ni_{0.5}Co_{0.5}Se$, $Ni_{0.8}Co_{0.2}Se$, NiSe, and CoSe in an $N_2$-saturated 1 M KOH solution obtained at a scan rate of 10 mV $s^{-1}$. **b** Tafel plots of the $Ni_{0.2}Co_{0.8}Se$, $Ni_{0.5}Co_{0.5}Se$, $Ni_{0.8}Co_{0.2}Se$, NiSe, and CoSe catalysts for the OER in 1.0 M KOH. **c** EIS Nyquist plots, where Rs represents the electrolyte resistance, C represents the double-layer capacitance, and $R_{ct}$ represents the charge-transfer resistance. **d** Chronoamperometric response of $Ni_{0.2}Co_{0.8}Se$ nanocages. The inset shows the LSV curves of an $Ni_{0.2}Co_{0.8}Se$ electrode tested after 1 and 1000 CV cycles

overpotential of 24.4 mV was needed to obtain a current density of 10 mA $cm^{-2}$.

### 3.4 HER Performance

Next, the $Ni_xCo_{1-x}Se$ samples were subjected to an HER test (Table 1). Figure 5a presents the LSV curves. To obtain a current density of 10 mA $cm^{-2}$, the required overpotential was 73, 112, 93, 150, and 99 mV for $Ni_{0.2}Co_{0.8}Se$, $Ni_{0.5}Co_{0.5}Se$, $Ni_{0.8}Co_{0.2}Se$, NiSe, and CoSe, respectively. NiSe exhibited the weakest catalytic activity, and the performance of CoSe was inferior to that of $Ni_{0.8}Co_{0.2}Se$ and $Ni_{0.2}Co_{0.8}Se$, in contrast to the results of the OER test. The best HER performance was exhibited by the $Ni_{0.2}Co_{0.8}Se$ sample, whose activity was close to that of the benchmark Pt/C catalyst for the HER (Fig. S7, overpotential of 38.1 mV at 10 mA $cm^{-2}$). The Tafel plots of the samples are presented in Fig. 5b, and the Tafel slopes were calculated. The Tafel slope was 54.8, 148.4, 86.8, 176.2, and 114.9 mV $dec^{-1}$ for $Ni_{0.2}Co_{0.8}Se$, $Ni_{0.5}Co_{0.5}Se$, $Ni_{0.8}Co_{0.2}Se$, NiSe, and CoSe, respectively. This trend matches the aforementioned overpotential values. $Ni_{0.2}Co_{0.8}Se$ exhibited the lowest Tafel slope value, indicating that it had the fastest reaction kinetics. Its Tafel slope is close to that of Pt/C (40.3 mV $dec^{-1}$), suggesting that a Tafel–Volmer mechanism occurred and that the rate-determining step in the HER was probably the electrochemical desorption of $H_2$ [50, 51]. Figure 5c shows the electrochemical impedance spectra of the samples. As anticipated, NiSe exhibited the largest semicircle. $Ni_{0.2}Co_{0.8}Se$ exhibited the smallest semicircle, indicating that it had the lowest electron-transfer resistance, which agrees well

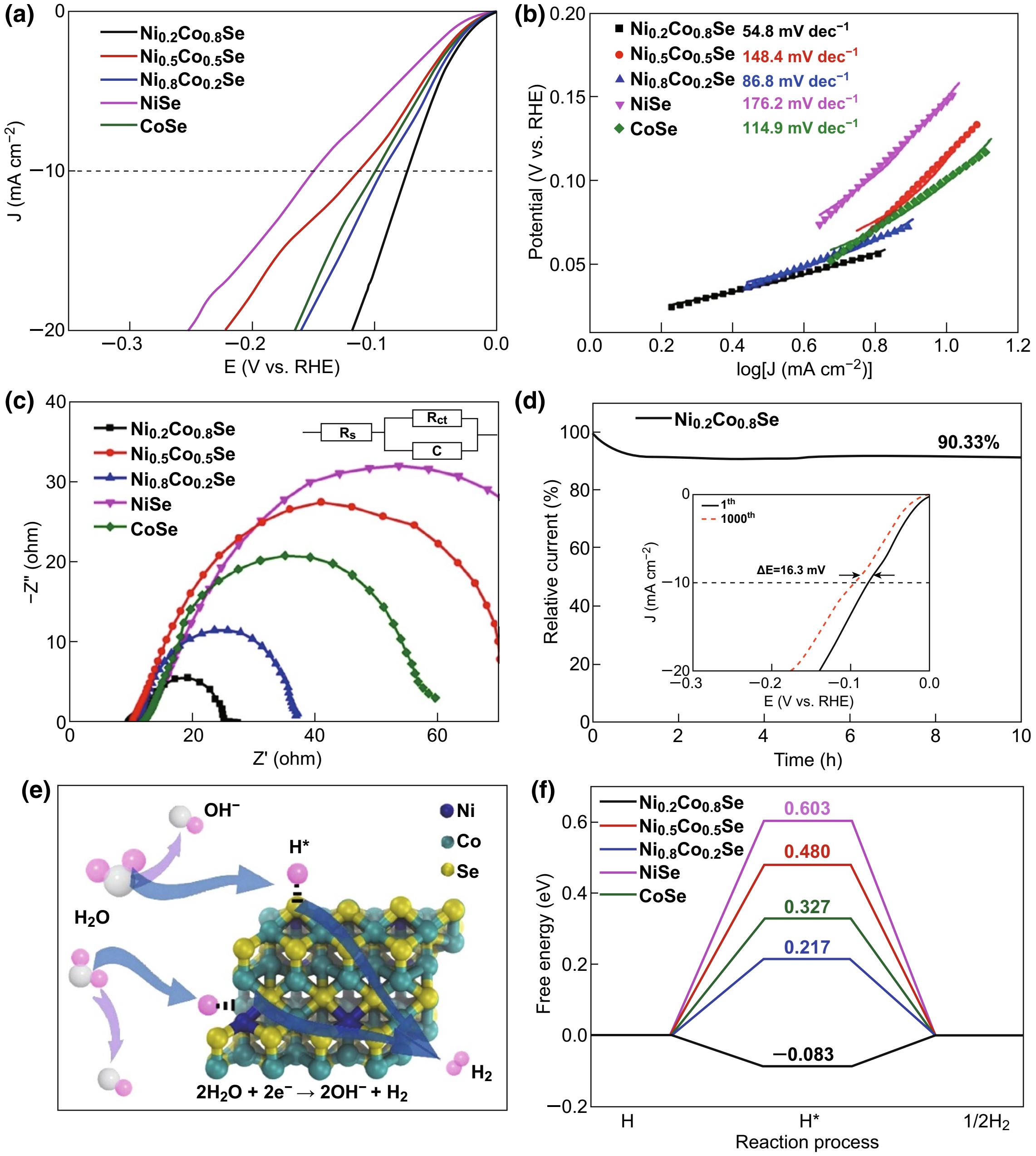

**Fig. 5** **a** HER polarization curves of $Ni_{0.2}Co_{0.8}Se$, $Ni_{0.5}Co_{0.5}Se$, $Ni_{0.8}Co_{0.2}Se$, NiSe, and CoSe obtained at a scan rate of 10 mV $s^{-1}$ in 1.0 M KOH. **b** Corresponding Tafel plots. **c** EIS Nyquist plots, where $R_s$ represents the electrolyte resistance, $C$ represents the double-layer capacitance, and $R_{ct}$ represents the charge-transfer resistance. **d** HER polarization curves of the $Ni_{0.2}Co_{0.8}Se$ electrode tested after 1 and 1000 CV cycles. The inset shows the chronoamperometric response of $Ni_{0.2}Co_{0.8}Se$ at 10 mA $cm^{-2}$. **e** Schematic of the HER at the $Ni_{0.2}Co_{0.8}Se$ active interface in the alkaline environment. **f** Adsorption free energy diagram for the Volmer reaction steps

with its high HER activity. Finally, the long-term stability of the samples was tested via both *i*–*t* measurements and an ADT. As illustrated in Fig. 5d, after continuous testing for approximately 10 h, 90.33% of the initial current was retained in the chronoamperometric measurement. The inset shows that after 1000 cycles of potential scans, at the current density of 10 mA $cm^{-2}$, the overpotential only shifted by 16.3 mV. Both tests indicate the robust stability of the $Ni_{0.2}Co_{0.8}Se$ sample in the long-term operation for the HER. To determine the reason for the high activity of $Ni_xCo_{1-x}Se$

toward the HER, the Gibbs free energy of H adsorption was calculated using the Norskov scheme (see details in Supplementary Material). First, the H adsorption free energy on the surface of pure NiSe(101) and CoSe(101) was calculated. Then, to elucidate the interplay between the Ni and Co dopants, models of the Ni-doped CoSe bulk material and the Co-doped NiSe bulk material with corresponding Co-to-Ni ratios were constructed, and all possible adsorption sites on the (101) planes were examined. Figure 5e illustrates the HER principle for the theoretical calculations under alkaline conditions, accompanied by the active sites of $Ni_{0.2}Co_{0.8}Se$. The active sites of the other samples are shown in Fig. S8. According to the reaction pathways, the enthalpies of the rate-determining Volmer step on the $Ni_xCo_{1-x}Se$ (101) surfaces were determined. For hydrogen adsorption, as shown in Fig. 5f, $Ni_{0.2}Co_{0.8}Se$ exhibited the lowest Gibbs free energy among the samples. The simulation results are in good accordance with the experimental results, providing theoretical evidence that $Ni_{0.2}Co_{0.8}Se$ has the best HER performance among the samples in the series.

### 3.5 EASA Analysis and ORR Performance

The OER and HER performance of the $Ni_{0.2}Co_{0.8}Se$ sample is comparable, if not superior, to that of most recently reported transition metal selenide-based materials, and the comparison results are presented in Table S1. For instance, in 1 M KOH for the OER, to obtain a current density of 10 mA $cm^{-2}$, the required overpotential of $Ni_{0.2}Co_{0.8}Se$ was 280 mV, which is lower than those for $CoSe_2/Mn_3O_4$ (450 mV) [52], $Ni_xSe$ (330 mV) [33], $Co_{0.85}Se$ (320 mV) [34], and $NiSe_2/Ti$ (295 mV) [53] and comparable to those for $Co(S_{0.22}Se_{0.78})_2$ (283 mV) [54], $Ni_{0.75}Fe_{0.25}Se_2$ (272 mV) [36], and NiSe/NF (270 mV) [55]. In the HER test, at 10 mA $cm^{-2}$, the overpotential was 73 mV for $Ni_{0.2}Co_{0.8}Se$, which is significantly lower than those for $Ni_xSe$ (233 mV) [33], $Co_{0.85}Se$ (230 mV) [34], $Co(S_{0.22}Se_{0.78})_2$ (175 mV) [54], and NiSe/NF (96 mV) [55] and comparable to that for $NiSe_2/Ti$ (70 mV) [53] under the same conditions. These comparison results indicate that $Ni_{0.2}Co_{0.8}Se$ is a superior multifunctional catalyst for the OER and HER.

To determine the reason for the difference in electrocatalytic activity among the samples, EASA measurements were taken [43]. The EASA values were estimated according to the electrochemical double-layer capacitance ($C_{DL}$) of the catalyst, and the $C_{DL}$ was measured via cyclic voltammograms (Fig. S9) within a potential range where no apparent Faradaic process occurred. The detailed calculations are presented in Supplementary Material, and the calculation results are presented in Table 1. The EASA values well explain the trend of the electrocatalytic performance, as they are in good accordance with the OER activity order of the series ($Ni_{0.2}Co_{0.8}Se > CoSe > Ni_{0.8}Co_{0.2}Se > Ni_{0.5}Co_{0.5}Se > NiSe$). The EASA of $Ni_{0.2}Co_{0.8}Se$ was the largest among the samples and was approximately 10 times larger than those of $Ni_{0.8}Co_{0.2}Se$ and $Ni_{0.5}Co_{0.5}Se$.

In addition, the ORR performance of the $Ni_xCo_{1-x}Se$ series was evaluated in an alkaline solution. Figure S10 shows the LSV polarization curves obtained with a rotation rate of 1600 rpm in 0.1 M KOH. The ORR activity matched the trend of the EASA values. As expected, the $Ni_{0.2}Co_{0.8}Se$ sample had the best activity in the series. Its onset potential was 0.87 V, and its diffusion-limiting current density was 4.45 mA $cm^{-2}$. Although its half-wave potential (0.769 V) was inferior to that of the commercial Pt/C (0.86 V), its limiting current density was higher than that of Pt/C (4.32 mA $cm^{-2}$). A large anode peak appeared at approximately 1.0 V, which was mainly due to the oxidation of the metal ions. A corresponding reduction peak appeared at approximately 0.7 V, which is ascribed to the reduction of $Ni^{3+}$ ($Co^{3+}$) to $Ni^{2+}$ ($Co^{2+}$) [56]. Additionally, there was a broad peak caused by the oxidation or reduction of surface Se, which was observed in previous studies [57, 58].

### 3.6 ZAB Performance

Inspired by the excellent performance of $Ni_{0.2}Co_{0.8}Se$ toward the OER and HER, we investigated its practical applicability by employing it as a multifunctional electrocatalyst for a ZAB and for overall water splitting. First, a proof-of-concept liquid ZAB was assembled (Fig. S11), which comprised $Ni_{0.2}Co_{0.8}Se$ as the air–cathode, a Zn plate as the anode, and 0.2 M ZnAc + 6 M KOH as the electrolyte [51, 59]. The reactions between the anode and the cathode during the charging and discharging of the ZAB are expressed as Eqs. 8–12 [60].

$$\text{Anode}: \mathrm{Zn} + 4\mathrm{OH}^- \rightarrow \mathrm{Zn(OH)}_4^{2-} + 2\mathrm{e}^- \tag{8}$$

$$\mathrm{Zn(OH)}_4^{2-} \rightarrow \mathrm{ZnO} + \mathrm{H_2O} + 2\mathrm{OH}^- \tag{9}$$

$$\text{Cathode}: \mathrm{O_2} + 4\mathrm{e}^- + 2\mathrm{H_2O} \rightarrow 4\mathrm{OH}^- \tag{10}$$

$$\text{Overall reaction}: \ 2\text{Zn} + \text{O}_2 \rightarrow 2\text{ZnO} \quad (11)$$

$$\text{Parasitic reaction}: \ \text{Zn} + 2\text{H}_2\text{O} \rightarrow \text{Zn(OH)}_2 + \text{H}_2 \quad (12)$$

The ZAB based on the $Ni_{0.2}Co_{0.8}Se$ air–cathode exhibited a stable open-circuit voltage of 1.44 V, which is close to that of the Pt/C + $RuO_2$ electrode (1.46 V) (Fig. S12), indicating that its performance is at least comparable to that of the conventional precious metal-based Pt/C + $RuO_2$ catalyst. The $Ni_{0.2}Co_{0.8}Se$ exhibited the highest open-circuit potential in the series (Fig. S12). The undulating charge–discharge voltages of $Ni_{0.2}Co_{0.8}Se$ and Pt/C + $RuO_2$ are shown in Fig. 6a. With continuous testing for over 50 h, the voltage gap of $Ni_{0.2}Co_{0.8}Se$ remained at approximately 0.873 V, which is comparable to that of the Pt/C + $RuO_2$ catalyst (0.845 V). For $Ni_{0.2}Co_{0.8}Se$, the initial round-trip efficiency at 5 h was 61.04%, and after 50 h of constant current charge–discharge cycles, the round-trip efficiency was 60.86% with no attenuation of the performance, which is superior to that of Pt/C + $RuO_2$ (58.91%) at 50 h. Furthermore, as indicated by the galvanostatic charge–discharge curves of the $Ni_xCo_{1-x}Se$ samples (Fig. S13a), only $Ni_{0.2}Co_{0.8}Se$ maintained a high stability and minimal voltage gap after 50 h of continuous operation. Thus, $Ni_{0.2}Co_{0.8}Se$ has excellent charge–discharge performance and stability. Figure 6b shows the charge–discharge polarization curves of rechargeable ZABs using $Ni_{0.2}Co_{0.8}Se$ and Pt/C + $RuO_2$. $Ni_{0.2}Co_{0.8}Se$ (0.9436 V) exhibited a smaller voltage gap than Pt/C + $RuO_2$ (0.9638 V) at the current density of 50 mA $cm^{-2}$, indicating that it had a higher charge–discharge capacity. The charge–discharge polarization curves (Fig. S13b) of $Ni_{0.5}Co_{0.5}Se$, $Ni_{0.8}Co_{0.2}Se$, NiSe, and CoSe show that the voltage gaps were 1.160, 1.186, 1.347, and 1.157 V, respectively, at the current density of 50 mA $cm^{-2}$. $Ni_{0.2}Co_{0.8}Se$ exhibited the smallest voltage gap, indicating its excellent charge–discharge performance. Moreover, the discharge and corresponding power density curves are presented in Fig. 6c. $Ni_{0.2}Co_{0.8}Se$ had a high power density of 223.5 mW $cm^{-2}$, which is higher than that of the Pt/C + $RuO_2$ catalyst (210.4 mW $cm^{-2}$), indicating its superiority for practical ZAB applications. Figure S13c shows that the maximum power density of $Ni_{0.5}Co_{0.5}Se$, $Ni_{0.8}Co_{0.2}Se$, NiSe, and CoSe was 153.8, 160.3, 134.4, and 181.3 mW $cm^{-2}$, respectively. All of these values are lower than that of $Ni_{0.2}Co_{0.8}Se$. Thus, $Ni_{0.2}Co_{0.8}Se$ had the highest discharge power density in the $Ni_xCo_{1-x}Se$ series. Figure S13d depicts the typical galvanostatic discharge profile at the current density of 10 mA $cm^{-2}$ with $Ni_xCo_{1-x}Se$ as the air–cathode. The specific capacity normalized to the weight of the consumed Zn plate was 698.6, 685.9, 664.8, 553.1, and 620.5 mAh $g^{-1}$ for $Ni_{0.2}Co_{0.8}Se$, $Ni_{0.5}Co_{0.5}Se$, $Ni_{0.8}Co_{0.2}Se$, NiSe, and CoSe, respectively. $Ni_{0.2}Co_{0.8}Se$ exhibited the best performance. Given the excellent performance of $Ni_{0.2}Co_{0.8}Se$ in the primary liquid ZAB, a portable, simple, and industrialized all-solid-state ZAB was fabricated, and the performance of $Ni_{0.2}Co_{0.8}Se$ in this device was examined. Figure 6d shows a schematic of the all-solid-state ZAB, and the fabrication steps are presented in Fig. S14. Figure 6e shows that the all-solid-state ZAB had a significant cycle life with an initial voltage gap of 0.71 V. After 240 cycles, the round-trip efficiency was attenuated from 61.96 to 55.26%. The efficiency decay of only 6.7% confirms the excellent stability of the all-solid-state ZAB using $Ni_{0.2}Co_{0.8}Se$. Owing to the high contact resistance of the battery components and the poor conductivity of the sand-absorbing alkaline PVA electrolyte, the all-solid-state ZAB was slightly less efficient than the liquid ZAB [61]. The charging and discharging polarization curves of the all-solid-state ZAB are presented in Fig. 6f. At the current density of 20 mA $cm^{-2}$, the voltage gap was 0.87 V, indicating outstanding charging and discharging performance. Figure 6g shows the polarization curves. The power density of the $Ni_{0.2}Co_{0.8}Se$-modified all-solid-state ZAB was calculated as 41.03 mW $cm^{-2}$. This battery also exhibited an impressive open-circuit potential of 1.428 V (Fig. 6h). Finally, we connected three all-solid-state ZABs in series with an open-circuit voltage of approximately 4.36 V (Fig. S15) and thus powered a board that illuminated light-emitting diodes (LEDs) with "SCUT" symbols (Fig. 6i).

The performance of $Ni_{0.2}Co_{0.8}Se$ in both the liquid ZAB and the all-solid-state ZAB was superior to that of the recently reported Co-based nanostructures. The comparison results are presented in Table S2. In the liquid ZAB test under the same conditions, the open-circuit potential for $Ni_{0.2}Co_{0.8}Se$ was higher than those for Co-NDC [62] and NGM-Co [63], and the power density was higher than those for $CoN_4$/NG [64], NGM-Co [63], and Co-NDC [62]. In the all-solid-state ZAB test, the open-circuit potential for $Ni_{0.2}Co_{0.8}Se$ was higher than those for NC-Co/$CoN_x$ [65], Co-NDC [62], and $Co_3O_4$/N-rGO [29]; the round-trip efficiency was higher than that for $CoN_4$/NG [64]; and the power density was higher than those for $CoN_4$/NG [64], NGM-Co [63], and $Co_3O_4$/N-rGO [29]. The outstanding performance of $Ni_{0.2}Co_{0.8}Se$ in the ZAB test is largely attributed

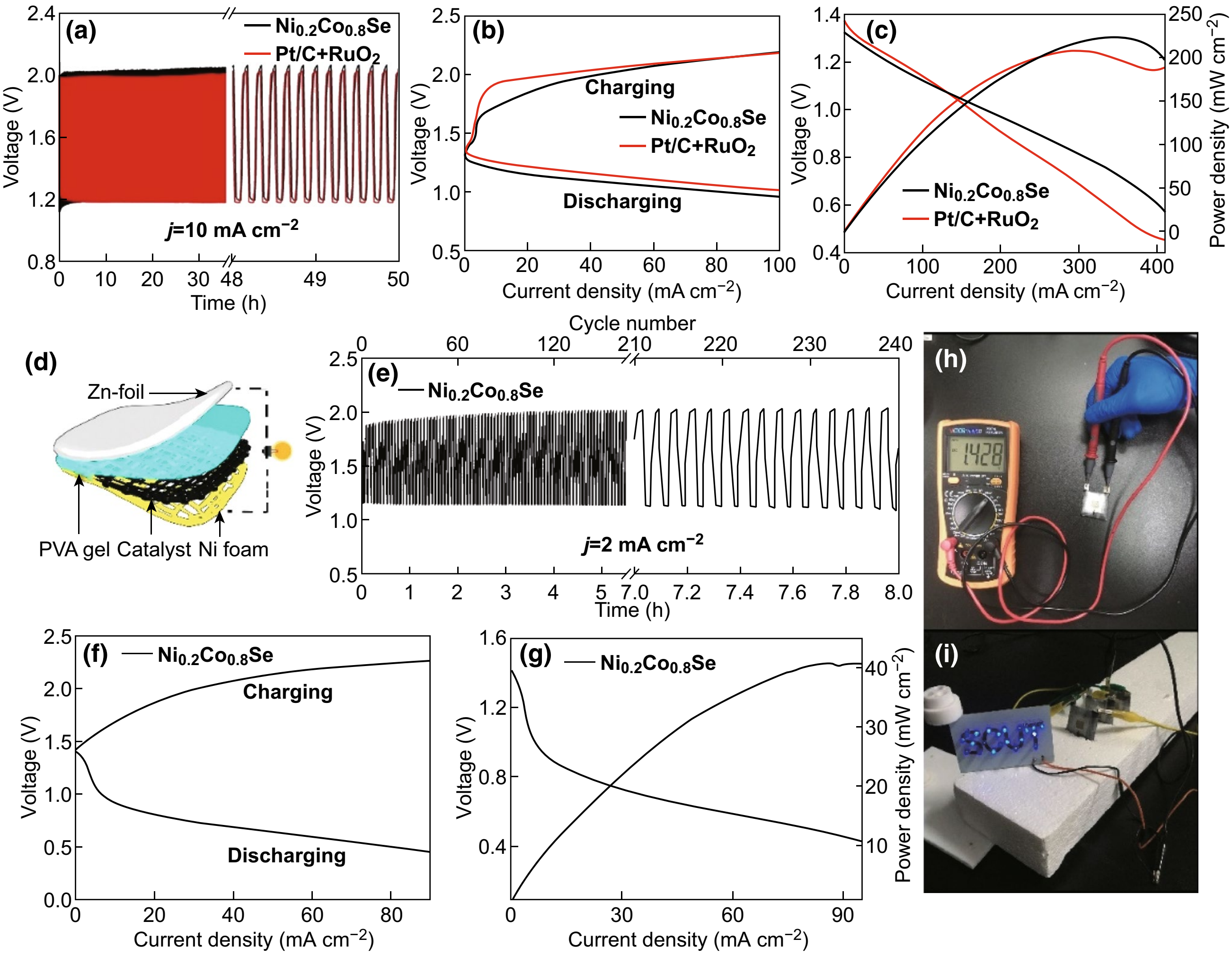

**Fig. 6** **a** Cycling performance of the rechargeable ZAB using $Ni_{0.2}Co_{0.8}Se$ at 10 mA cm$^{-2}$, where each cycle lasted 5 min. **b** Charge–discharge polarization curves of the rechargeable ZABs using $Ni_{0.2}Co_{0.8}Se$ and Pt/C + $RuO_2$. **c** Polarization and power density curves of the ZABs using the $Ni_{0.2}Co_{0.8}Se$ and Pt/C + $RuO_2$ catalysts. **d** Schematic of the self-made all-solid-state ZAB. **e** Cycling performance of the all-solid-state ZAB using $Ni_{0.2}Co_{0.8}Se$ at 2 mA cm$^{-2}$, where each cycle lasted 2 min. **f** Charge–discharge polarization curves of the all-solid-state ZAB using $Ni_{0.2}Co_{0.8}Se$. **g** Polarization and power density curves of the all-solid-state ZAB using $Ni_{0.2}Co_{0.8}Se$. **h** Open-circuit voltage of an all-solid-state ZAB and **i** an LED circuit board powered by three all-solid-state ZABs

to its excellent electrocatalytic performance, as discussed previously.

### 3.7 Overall Water-Splitting Test

Next, $Ni_{0.2}Co_{0.8}Se$ was employed for overall water splitting in an alkalic solution, in comparison with the Pt/C + $RuO_2$ catalyst [51, 66, 67]. $Ni_{0.2}Co_{0.8}Se$ was used as the catalyst in both the cathode and the anode. In a control experiment, Pt/C was used as the cathode catalyst, and $RuO_2$ was employed as the anode catalyst. Figure 7a presents the water-splitting polarization curves of $Ni_{0.2}Co_{0.8}Se$ and Pt/C + $RuO_2$ in a 1 M KOH solution. For obtaining a current density of 10 mA cm$^{-2}$, the required cell voltage was 1.592 V for $Ni_{0.2}Co_{0.8}Se$, which is significantly lower than that for the Pt/C + $RuO_2$ catalyst (1.628 V). Thus, $Ni_{0.2}Co_{0.8}Se$ had a better water-splitting capability than the combined precious metal-based standard catalyst in the alkaline solution. The long-term durability of the $Ni_{0.2}Co_{0.8}Se$ sample was evaluated via chronoamperometric measurement for 50,000 s. As shown in Fig. 7b, after constant water-splitting operation for approximately 13 h, $Ni_{0.2}Co_{0.8}Se$ retained 78.5% of its initial

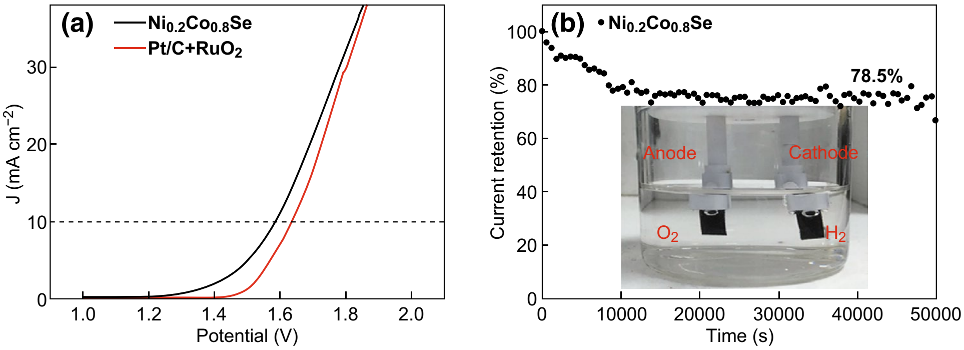

**Fig. 7** **a** Water-splitting polarization curves of $Ni_{0.2}Co_{0.8}Se$ and Pt/C + $RuO_2$ in 1 M KOH. **b** Chronoamperometric response of $Ni_{0.2}Co_{0.8}Se$ nanocages for overall water splitting. The inset shows the gas evolution on the two electrodes at 10 mA $cm^{-2}$

current. The inset shows that $H_2$ and $O_2$ bubbles were visible at the cathode and anode, respectively. These findings confirm that $Ni_{0.2}Co_{0.8}Se$ is a promising high-efficiency, cost-effective electrocatalyst for overall water-splitting devices in alkaline solutions.

## 4 Conclusions

We demonstrated the facile fabrication of a series of $Ni_xCo_{1-x}Se$ samples with well-defined cages and investigated their catalytic performance for OER, HER, and ORR electrocatalysis. Among the $Ni_xCo_{1-x}Se$ compounds, $Ni_{0.2}Co_{0.8}Se$ exhibited the best performance, as indicated by the lowest overpotential of 280 and 73 mV to obtain a current density of 10 mA $cm^{-2}$ for the OER and HER, respectively. Moreover, $Ni_{0.2}Co_{0.8}Se$ was engineered as an air–cathode of both a rechargeable ZAB and an all-solid-state ZAB and employed as a catalyst for overall water splitting. It endowed both ZAB devices with outstanding performance, including a long cycling lifetime, high round-trip efficiency, and high power density, and achieved total water splitting with excellent efficiency at a low cell voltage. The study paves a pathway for preparing transition metal selenides with a well-defined morphology and optimized stoichiometric ratio as promising catalysts for renewable energy technologies, such as rechargeable and all-solid-state metal–air batteries and water-splitting devices.

**Acknowledgements** Z. Tang thanks the Guangzhou Science and Technology Plan Projects (No. 201804010323), the Guangdong Natural Science Funds for Distinguished Young Scholars (No. 2015A030306006), the Guangdong Innovative and Entrepreneurial Research Team Program (No. 2014ZT05N200), and the Fundamental Research Funds for the Central Universities (SCUT Grant No. 2018ZD022). Y. Tian is grateful for the Project for Natural Science Foundation of Guangdong Province (No. 2018A030313178), and W. Gao thanks the funding support from the Natural Science Foundation of Guangdong Province (No. 2015A030310176).

---

**Electronic supplementary material** The online version of this article (https://doi.org/10.1007/s40820-019-0258-0) contains supplementary material, which is available to authorized users.

---

## References

1. Y. Li, H. Dai, Recent advances in zinc-air batteries. Chem. Soc. Rev. **43**(15), 5257–5275 (2014). https://doi.org/10.1039/C4CS00015C
2. J. Yin, Y. Li, F. Lv, M. Lu, K. Sun, W. Wang et al., Oxygen vacancies dominated $NiS_2$/$CoS_2$ interface porous nanowires for portable Zn–air batteries driven water splitting devices. Adv. Mater. **29**(47), 1704681 (2017). https://doi.org/10.1002/adma.201704681
3. X. Chen, Z. Zhang, L. Chi, A.K. Nair, W. Shangguan, Z. Jiang, Recent advances in visible-light-driven photoelectrochemical water splitting: catalyst nanostructures and reaction systems. Nano-Micro Lett. **8**(1), 1–12 (2016). https://doi.org/10.1007/s40820-015-0063-3
4. Q. Zhao, Z. Yan, C. Chen, J. Chen, Spinels: controlled preparation, oxygen reduction/evolution reaction application, and beyond. Chem. Rev. **117**(15), 10121–10211 (2017). https://doi.org/10.1021/acs.chemrev.7b00051

5. K. Liang, L. Guo, K. Marcus, S. Zhang, Z. Yang et al., Overall water splitting with room-temperature synthesized nife oxyfluoride nanoporous films. ACS Catal. **7**(12), 8406–8412 (2017). https://doi.org/10.1021/acscatal.7b02991
6. J. Li, W. Xu, J. Luo, D. Zhou, D. Zhang, L. Wei, P. Xu, D. Yuan, Synthesis of 3d hexagram-like cobalt–manganese sulfides nanosheets grown on nickel foam: a bifunctional electrocatalyst for overall water splitting. Nano-Micro Lett. **10**(1), 6 (2017). https://doi.org/10.1007/s40820-017-0160-6
7. X. Han, X. Wu, Y. Deng, J. Liu, J. Lu, C. Zhong, W. Hu, Ultrafine pt nanoparticle-decorated pyrite-type $CoS_2$ nanosheet arrays coated on carbon cloth as a bifunctional electrode for overall water splitting. Adv. Energy Mater. **8**(24), 1800935 (2018). https://doi.org/10.1002/aenm.201800935
8. M. Liu, R. Zhang, W. Chen, Graphene-supported nanoelectrocatalysts for fuel cells: synthesis, properties, and applications. Chem. Rev. **114**(10), 5117–5160 (2014). https://doi.org/10.1021/cr400523y
9. M. Shao, Q. Chang, J.-P. Dodelet, R. Chenitz, Recent advances in electrocatalysts for oxygen reduction reaction. Chem. Rev. **116**(6), 3594–3657 (2016). https://doi.org/10.1021/acs.chemrev.5b00462
10. L. Wang, Z. Tang, W. Yan, Q. Wang, H. Yang, S. Chen, Co@pt core@shell nanoparticles encapsulated in porous carbon derived from zeolitic imidazolate framework 67 for oxygen electroreduction in alkaline media. J. Power Sour. **343**, 458–466 (2017). https://doi.org/10.1016/j.jpowsour.2017.01.081
11. D. Strmcnik, P.P. Lopes, B. Genorio, V.R. Stamenkovic, N.M. Markovic, Design principles for hydrogen evolution reaction catalyst materials. Nano Energy **29**, 29–36 (2016). https://doi.org/10.1016/j.nanoen.2016.04.017
12. J. Wang, F. Xu, H. Jin, Y. Chen, Y. Wang, Non-noble metal-based carbon composites in hydrogen evolution reaction: fundamentals to applications. Adv. Mater. **29**(14), 1605838 (2017). https://doi.org/10.1002/adma.201605838
13. L.C. Seitz, C.F. Dickens, K. Nishio, Y. Hikita, J. Montoya et al., A highly active and stable $IrO_x/SrIrO_3$ catalyst for the oxygen evolution reaction. Science **353**(6303), 1011–1014 (2016). https://doi.org/10.1126/science.aaf5050
14. T. Reier, M. Oezaslan, P. Strasser, Electrocatalytic oxygen evolution reaction (OER) on Ru, Ir, and Pt catalysts: a comparative study of nanoparticles and bulk materials. ACS Catal. **2**(8), 1765–1772 (2012). https://doi.org/10.1021/cs3003098
15. W. Niu, L. Li, X. Liu, N. Wang, J. Liu, W. Zhou, Z. Tang, S. Chen, Mesoporous *n*-doped carbons prepared with thermally removable nanoparticle templates: an efficient electrocatalyst for oxygen reduction reaction. J. Am. Chem. Soc. **137**(16), 5555–5562 (2015). https://doi.org/10.1021/jacs.5b02027
16. G. Wu, J. Wang, W. Ding, Y. Nie, L. Li, X. Qi, S. Chen, Z. Wei, A strategy to promote the electrocatalytic activity of spinels for oxygen reduction by structure reversal. Angew. Chem. Int. Ed. **55**(4), 1340–1344 (2016). https://doi.org/10.1002/anie.201508809
17. Z.J. Xu, From two-phase to three-phase: the new electrochemical interface by oxide electrocatalysts. Nano-Micro Lett. **10**(1), 8 (2017). https://doi.org/10.1007/s40820-017-0161-5
18. H. Wang, N. Yang, W. Li, W. Ding, K. Chen et al., Understanding the roles of nitrogen configurations in hydrogen evolution: trace atomic cobalt boosts the activity of planar nitrogen-doped graphene. ACS Energy Lett. **3**(6), 1345–1352 (2018). https://doi.org/10.1021/acsenergylett.8b00522
19. L. Xu, Q. Jiang, Z. Xiao, X. Li, J. Huo, S. Wang, L. Dai, Plasma-engraved $Co_3O_4$ nanosheets with oxygen vacancies and high surface area for the oxygen evolution reaction. Angew. Chem. Int. Ed. **55**(17), 5277–5281 (2016). https://doi.org/10.1002/anie.201600687
20. W. Niu, S. Pakhira, K. Marcus, Z. Li, J.L. Mendoza-Cortes, Y. Yang, Apically dominant mechanism for improving catalytic activities of n-doped carbon nanotube arrays in rechargeable zinc–air battery. Adv. Energy Mater. **8**(20), 1800480 (2018). https://doi.org/10.1002/aenm.201800480
21. C. Lei, H. Chen, J. Cao, J. Yang, M. Qiu et al., Fe-$n_4$ sites embedded into carbon nanofiber integrated with electrochemically exfoliated graphene for oxygen evolution in acidic medium. Adv. Energy Mater. **8**(26), 1801912 (2018). https://doi.org/10.1002/aenm.201801912
22. D. Chen, M. Qiao, Y.-R. Lu, L. Hao, D. Liu, C.-L. Dong, Y. Li, S. Wang, Preferential cation vacancies in perovskite hydroxide for the oxygen evolution reaction. Angew. Chem. Int. Ed. **57**(28), 8691–8696 (2018). https://doi.org/10.1002/anie.201805520
23. Y. Wang, C. Xie, Z. Zhang, D. Liu, R. Chen, S. Wang, In situ exfoliated, n-doped, and edge-rich ultrathin layered double hydroxides nanosheets for oxygen evolution reaction. Adv. Funct. Mater. **28**(4), 1703363 (2018). https://doi.org/10.1002/adfm.201703363
24. S. Dou, X. Wang, S. Wang, Rational design of transition metal-based materials for highly efficient electrocatalysis. Small Methods (2018). https://doi.org/10.1002/smtd.201800211
25. Z. Song, X. Han, Y. Deng, N. Zhao, W. Hu, C. Zhong, Clarifying the controversial catalytic performance of $Co(OH)_2$ and $Co_3O_4$ for oxygen reduction/evolution reactions toward efficient Zn–air batteries. ACS Appl. Mater. Interfaces **9**(27), 22694–22703 (2017). https://doi.org/10.1021/acsami.7b05395
26. X. Chen, B. Liu, C. Zhong, Z. Liu, J. Liu et al., Ultrathin $co_3o_4$ layers with large contact area on carbon fibers as high-performance electrode for flexible zinc–air battery integrated with flexible display. Adv. Energy Mater. **7**(18), 1700779 (2017). https://doi.org/10.1002/aenm.201700779
27. Z. Yang, J.-Y. Zhang, Z. Liu, Z. Li, L. Lv et al., “Cuju”-structured iron diselenide-derived oxide: a highly efficient electrocatalyst for water oxidation. ACS Appl. Mater. Interfaces. **9**(46), 40351–40359 (2017). https://doi.org/10.1021/acsami.7b14072
28. J.-Y. Zhang, H. Wang, Y. Tian, Y. Yan, Q. Xue et al., Anodic hydrazine oxidation assists energy-efficient hydrogen evolution over a bifunctional cobalt perselenide nanosheet electrode. Angew. Chem. Int. Ed. **57**(26), 7649–7653 (2018). https://doi.org/10.1002/anie.201803543
29. Y. Li, C. Zhong, J. Liu, X. Zeng, S. Qu et al., Atomically thin mesoporous $Co_3O_4$ layers strongly coupled with n-rgo

nanosheets as high-performance bifunctional catalysts for 1D knittable zinc–air batteries. Adv. Mater. **30**(4), 1703657 (2018). https://doi.org/10.1002/adma.201703657

30. Y. Liu, H. Cheng, M. Lyu, S. Fan, Q. Liu et al., Low overpotential in vacancy-rich ultrathin $CoSe_2$ nanosheets for water oxidation. J. Am. Chem. Soc. **136**(44), 15670–15675 (2014). https://doi.org/10.1021/ja5085157
31. A. Sivanantham, S. Shanmugam, Nickel selenide supported on nickel foam as an efficient and durable non-precious electrocatalyst for the alkaline water electrolysis. Appl. Catal. B Environ. **203**, 485–493 (2017). https://doi.org/10.1016/j.apcatb.2016.10.050
32. Z.-Q. Liu, H. Cheng, N. Li, T.Y. Ma, Y.Z. Su, $ZnCo_2O_4$ quantum dots anchored on nitrogen-doped carbon nanotubes as reversible oxygen reduction/evolution electrocatalysts. Adv. Mater. **28**(19), 3777–3784 (2016). https://doi.org/10.1002/adma.201506197
33. X. Zheng, X. Han, H. Liu, J. Chen, D. Fu, J. Wang, C. Zhong, Y. Deng, W. Hu, Controllable synthesis of nixse ($0.5 \leq x \leq 1$) nanocrystals for efficient rechargeable zinc–air batteries and water splitting. ACS Appl. Mater. Interfaces. **10**(16), 13675–13684 (2018). https://doi.org/10.1021/acsami.8b01651
34. T. Meng, J. Qin, S. Wang, D. Zhao, B. Mao, M. Cao, In situ coupling of $Co_{0.85}Se$ and n-doped carbon via one-step selenization of metal–organic frameworks as a trifunctional catalyst for overall water splitting and Zn–air batteries. J. Mater. Chem. A **5**(15), 7001–7014 (2017). https://doi.org/10.1039/C7TA01453H
35. X. Xu, F. Song, X. Hu, A nickel iron diselenide-derived efficient oxygen-evolution catalyst. Nat. Commun. **7**, 12324 (2016). https://doi.org/10.1038/ncomms12324
36. L. Lv, Z. Li, Y. Ruan, Y. Chang, X. Ao, J.-G. Li, Z. Yang, C. Wang, Nickel–iron diselenide hollow nanoparticles with strongly hydrophilic surface for enhanced oxygen evolution reaction activity. Electrochim. Acta **286**, 172–178 (2018). https://doi.org/10.1016/j.electacta.2018.08.039
37. L. Lv, Z. Li, K.-H. Xue, Y. Ruan, X. Ao et al., Tailoring the electrocatalytic activity of bimetallic nickel–iron diselenide hollow nanochains for water oxidation. Nano Energy **47**, 275–284 (2018). https://doi.org/10.1016/j.nanoen.2018.03.010
38. J.-Y. Zhang, L. Lv, Y. Tian, Z. Li, X. Ao, Y. Lan, J. Jiang, C. Wang, Rational design of cobalt–iron selenides for highly efficient electrochemical water oxidation. ACS Appl. Mater. Interfaces **9**(39), 33833–33840 (2017). https://doi.org/10.1021/acsami.7b08917
39. L. Hou, Y. Shi, C. Wu, Y. Zhang, Y. Ma et al., Monodisperse metallic $NiCoSe_2$ hollow sub-microspheres: formation process, intrinsic charge-storage mechanism, and appealing pseudocapacitance as highly conductive electrode for electrochemical supercapacitors. Adv. Funct. Mater. **28**(13), 1705921 (2018). https://doi.org/10.1002/adfm.201705921
40. J. Li, M. Wan, T. Li, H. Zhu, Z. Zhao, Z. Wang, W. Wu, M. Du, $NiCoSe_{2-x}/n$-doped C mushroom-like core/shell nanorods on n-doped carbon fiber for efficiently electrocatalyzed overall water splitting. Electrochim. Acta **272**, 161–168 (2018). https://doi.org/10.1016/j.electacta.2018.04.032
41. T. Chen, Y. Tan, Hierarchical $CoNiSe_2$ nano-architecture as a high-performance electrocatalyst for water splitting. Nano Res. **11**(3), 1331–1344 (2018). https://doi.org/10.1007/s12274-017-1748-3
42. H. Zhu, R. Jiang, X. Chen, Y. Chen, L. Wang, 3D nickel–cobalt diselenide nanonetwork for highly efficient oxygen evolution. Sci. Bull. **62**(20), 1373–1379 (2017). https://doi.org/10.1016/j.scib.2017.09.012
43. B. Qiu, L. Cai, Y. Wang, Z. Lin, Y. Zuo, M. Wang, Y. Chai, Fabrication of nickel–cobalt bimetal phosphide nanocages for enhanced oxygen evolution catalysis. Adv. Funct. Mater. **28**(17), 1706008 (2018). https://doi.org/10.1002/adfm.201706008
44. Z. Fang, L. Peng, Y. Qian, X. Zhang, Y. Xie, J.J. Cha, G. Yu, Dual tuning of Ni–Co–a ($a = $ P, Se, O) nanosheets by anion substitution and holey engineering for efficient hydrogen evolution. J. Am. Chem. Soc. **140**(15), 5241–5247 (2018). https://doi.org/10.1021/jacs.8b01548
45. T. Gong, R. Qi, X. Liu, H. Li, Y. Zhang, N, f-codoped microporous carbon nanofibers as efficient metal-free electrocatalysts for ORR. Nano-Micro Lett. **11**(1), 9 (2019). https://doi.org/10.1007/s40820-019-0240-x
46. Z.-W. Gao, J.-Y. Liu, X.-M. Chen, X.-L. Zheng, J. Mao et al., Engineering NiO/NiFe LDH intersection to bypass scaling relationship for oxygen evolution reaction via dynamic tridimensional adsorption of intermediates. Adv. Mater. (2019). https://doi.org/10.1002/adma.201804769
47. X. Han, X. Wu, C. Zhong, Y. Deng, N. Zhao, W. Hu, $NiCo_2S_4$ nanocrystals anchored on nitrogen-doped carbon nanotubes as a highly efficient bifunctional electrocatalyst for rechargeable zinc–air batteries. Nano Energy **31**, 541–550 (2017). https://doi.org/10.1016/j.nanoen.2016.12.008
48. J. Nai, S. Wang, Y. Bai, L. Guo, Amorphous $Ni(OH)_2$ nanoboxes: fast fabrication and enhanced sensing for glucose. Small **9**(18), 3147–3152 (2013). https://doi.org/10.1002/smll.201203076
49. C.V.V. Muralee Gopi, A.E. Reddy, H.-J. Kim, Wearable superhigh energy density supercapacitors using a hierarchical ternary metal selenide composite of $CoNiSe_2$ microspheres decorated with $CoFe_2Se_4$ nanorods. J. Mater. Chem. A **6**(17), 7439–7448 (2018). https://doi.org/10.1039/C8TA01141A
50. J. Yin, Q. Fan, Y. Li, F. Cheng, P. Zhou, P. Xi, S. Sun, Ni–C–N nanosheets as catalyst for hydrogen evolution reaction. J. Am. Chem. Soc. **138**(44), 14546–14549 (2016). https://doi.org/10.1021/jacs.6b09351
51. Z. Ding, Z. Tang, L. Li, K. Wang, W. Wu, X. Chen, X. Wu, S. Chen, Ternary ptvco dendrites for the hydrogen evolution reaction, oxygen evolution reaction, overall water splitting and rechargeable Zn–air batteries. Inorg. Chem. Front. **5**(10), 2425–2431 (2018). https://doi.org/10.1039/C8QI00623G
52. M.-R. Gao, Y.-F. Xu, J. Jiang, Y.-R. Zheng, S.-H. Yu, Water oxidation electrocatalyzed by an efficient $Mn_3O_4/CoSe_2$ nanocomposite. J. Am. Chem. Soc. **134**(6), 2930–2933 (2012). https://doi.org/10.1021/ja211526y
53. Z. Pu, Y. Luo, A.M. Asiri, X. Sun, Efficient electrochemical water splitting catalyzed by electrodeposited nickel diselenide

nanoparticles based film. ACS Appl. Mater. Interfaces **8**(7), 4718–4723 (2016). https://doi.org/10.1021/acsami.5b12143

54. L. Fang, W. Li, Y. Guan, Y. Feng, H. Zhang, S. Wang, Y. Wang, Tuning unique peapod-like $Co(S_xSe_{1-x})_2$ nanoparticles for efficient overall water splitting. Adv. Funct. Mater. **27**(24), 1701008 (2017). https://doi.org/10.1002/adfm.201701008
55. C. Tang, N. Cheng, Z. Pu, W. Xing, X. Sun, NiSe nanowire film supported on nickel foam: an efficient and stable 3D bifunctional electrode for full water splitting. Angew. Chem. Int. Ed. **54**(32), 9351–9355 (2015). https://doi.org/10.1002/anie.201503407
56. Z. Deng, Q. Yi, Y. Zhang, H. Nie, G. Li, L. Yu, X. Zhou, Carbon paper-supported NiCo/C–N catalysts synthesized by directly pyrolyzing NiCo-doped polyaniline for oxygen reduction reaction. NANO **13**(1), 1850006 (2018). https://doi.org/10.1142/s1793292018500066
57. L. Timperman, A.S. Gago, N. Alonso-Vante, Oxygen reduction reaction increased tolerance and fuel cell performance of Pt and $Ru_xSe_y$ onto oxide–carbon composites. J. Power Sour. **196**(9), 4290–4297 (2011). https://doi.org/10.1016/j.jpowsour.2010.11.083
58. C. Delacôte, A. Lewera, M. Pisarek, P.J. Kulesza, P. Zelenay, N. Alonso-Vante, The effect of diluting ruthenium by iron in $Ru_xSe_y$ catalyst for oxygen reduction. Electrochim. Acta **55**(26), 7575–7580 (2010). https://doi.org/10.1016/j.electacta.2010.01.029
59. K. Wang, Z. Tang, W. Wu, P. Xi, D. Liu et al., Nanocomposites $CoPt-x$/diatomite-C as oxygen reversible electrocatalysts for zinc-air batteries: diatomite boosted the catalytic activity and durability. Electrochim. Acta **284**, 119–127 (2018). https://doi.org/10.1016/j.electacta.2018.07.154
60. X. Han, G. He, Y. He, J. Zhang, X. Zheng et al., Engineering catalytic active sites on cobalt oxide surface for enhanced oxygen electrocatalysis. Adv. Energy Mater. **8**(10), 1702222 (2018). https://doi.org/10.1002/aenm.201702222
61. I.S. Amiinu, Z. Pu, X. Liu, K.A. Owusu, H.G.R. Monestel, F.O. Boakye, H. Zhang, S. Mu, Multifunctional Mo–N/C@$MoS_2$ electrocatalysts for HER, OER, ORR, and Zn–air batteries. Adv. Funct. Mater. **27**(44), 1702300 (2017). https://doi.org/10.1002/adfm.201702300
62. Z. Chen, Q. Wang, X. Zhang, Y. Lei, W. Hu, Y. Luo, Y. Wang, N-doped defective carbon with trace Co for efficient rechargeable liquid electrolyte-/all-solid-state Zn–air batteries. Sci. Bull. **63**(9), 548–555 (2018). https://doi.org/10.1016/j.scib.2018.04.003
63. C. Tang, B. Wang, H.-F. Wang, Q. Zhang, Defect engineering toward atomic Co–$N_x$–C in hierarchical graphene for rechargeable flexible solid Zn–air batteries. Adv. Mater. **29**(37), 1703185 (2017). https://doi.org/10.1002/adma.201703185
64. L. Yang, L. Shi, D. Wang, Y. Lv, D. Cao, Single-atom cobalt electrocatalysts for foldable solid-state Zn–air battery. Nano Energy **50**, 691–698 (2018). https://doi.org/10.1016/j.nanoen.2018.06.023
65. C. Guan, A. Sumboja, W. Zang, Y. Qian, H. Zhang et al., Decorating Co/CoNx nanoparticles in nitrogen-doped carbon nanoarrays for flexible and rechargeable zinc–air batteries. Energy Storage Mater. **16**, 243–250 (2019). https://doi.org/10.1016/j.ensm.2018.06.001
66. D. Li, Z. Zong, Z. Tang, Z. Liu, S. Chen, Y. Tian, X. Wang, Total water splitting catalyzed by Co@Ir core–shell nanoparticles encapsulated in nitrogen-doped porous carbon derived from metal–organic frameworks. ACS Sustain. Chem. Eng. **6**(4), 5105–5114 (2018). https://doi.org/10.1021/acssuschemeng.7b04777
67. Y. Li, J. Yin, L. An, M. Lu, K. Sun, Y.-Q. Zhao, D. Gao, F. Cheng, P. Xi, $FeS_2/CoS_2$ interface nanosheets as efficient bifunctional electrocatalyst for overall water splitting. Small **14**(26), 1801070 (2018). https://doi.org/10.1002/smll.201801070